Small

NANO · MICRO small
www.small-journal.com

RESEARCH ARTICLE

Interface-Selective Charge Transport Enables Self-Powered Vertical WSe_2/Perovskite Photodetector Arrays

Jiaqi Tang[1,2,3,4] | Yang Yu[1] | Xiaojun Pan[1] | Yepei Mo[1,4] | Huichen Xu[2,3] | Jia Long[2,3] | Kaiyu Hu[2,3] | Yu Zhang[2,3] | Yipeng Cui[2,3] | Jiarun Ding[1,4] | Teng Gao[2,3] | Zhifang Liu[2,3] | Wenchao Gao[1,4] | Wenqiang Wu[2] | Muhong Wu[2,3] | Caofeng Pan[2,3]

[1]Beijing Institute of Nanoenergy and Nanosystems, Chinese Academy of Sciences, Beijing, P. R. China | [2]Beijing Key Laboratory for Atomic Manufacturing Equipment and Intelligent Sensing, Institute of Atomic Manufacturing, Beihang University, Beijing, P. R. China | [3]International Research Institute for Multidisciplinary Science, Beihang University, Beijing, P. R. China | [4]School of Nanoscience and Engineering, University of Chinese Academy of Sciences, Beijing, P. R. China

Correspondence: Wenchao Gao (gaowenchao@binn.cas.cn) | Wenqiang Wu (wuwenqiang@buaa.edu.cn) | Muhong Wu (muhongwu@buaa.edu.cn) | Caofeng Pan (pancaofeng@buaa.edu.cn)

Received: 4 March 2026 | **Revised:** 17 April 2026 | **Accepted:** 29 April 2026

Keywords: heterostructures | imaging | photodetectors | self-powered

ABSTRACT

Self-powered photodetectors operating at zero bias are highly attractive for low-power integrated optoelectronic systems, yet their performance is often limited by inefficient carrier extraction and severe interfacial recombination in 2D/3D heterostructures. Here, we report a vertical Au/WSe_2/$MAPbBrI_2$/ZnO/ITO photodetector array enabled by interface-selective charge transport engineering. By integrating p-type WSe_2 with a strongly absorbing mixed-halide perovskite and introducing ZnO as an electron transport layer, a favorable energy cascade is formed, which is consistent with selective carrier separation under zero bias. Comparative studies reveal that the ZnO interlayer significantly suppresses dark current, enhances rectification behavior, and improves zero-bias photocurrent by facilitating selective electron extraction and suppressing interfacial recombination. The optimized device exhibits stable switching characteristics and uniform pixel-to-pixel response, enabling reliable self-powered imaging. This work clarifies the critical role of transport-layer-assisted interface modulation in vertical 2D/3D heterojunctions and provides a scalable strategy for constructing high-performance, energy-efficient photodetector arrays.

1 | Introduction

Photodetectors have become indispensable components in quantum communication [1], autonomous control [2], clinical imaging [3, 4], and intelligent sensing networks [5–7], owing to their high-efficiency photoelectric conversion capabilities [8–11]. Nevertheless, the heavy reliance on external power bias inevitably introduces systemic complexity, elevated power consumption, and thermal noise, which collectively impede the evolution of photodetection systems toward miniaturization, high-density pixel integration, and high-precision instrumentation [12–14]. Consequently, self-powered photodetectors operating at zero bias have emerged as a focal point of research, offering a sustainable trajectory toward next-generation low-power integrated optoelectronic technologies [15–17]. Among diverse structural configurations, vertical heterojunctions exhibit superior performance over their planar counterparts, characterized by abbreviated carrier transport pathways, robust built-in electric fields, and

---

Jiaqi Tang and Yang Yu contributed equally to this work.

enhanced scalability for large-scale array integration [18–20]. These intrinsic merits not only optimize spatial utilization but also establish vertical architectures as an ideal paradigm for high-performance self-powered photodetection.

Two-dimensional (2D) transition metal dichalcogenides (TMDs) have garnered immense interest due to their atomic-level thickness, dangling-bond-free interfaces, and exceptional charge transport properties, positioning them as premier candidates for post-Moore integrated circuits [21–25]. Among them, MoS_2 and WSe_2, as typical n-type and p-type semiconductors respectively, have shown unique advantages in constructing heterojunctions for photodetection, such as high carrier mobility and tunable bandgaps in the visible to near-infrared range [26–28]. However, due to their ultrathin structure, 2D materials have limited light absorption capacity, resulting in slow response speed and weak photodetection ability, which seriously restricts their application in vertical structure self-powered detectors [29]. The inherent flexibility of 2D materials to form van der Waals (vdW) heterostructures enables the seamless integration of high-extinction-coefficient media [30]. This structure has become a key approach to overcoming the limited light-matter interaction in the original two-dimensional layer, thereby significantly enhancing its photoelectric conversion efficiency [31]. Organic-inorganic hybrid lead halide perovskites possess excellent photoelectric properties, including high absorption coefficient, high carrier mobility, long carrier diffusion length, and tunable optical bandgaps, providing the possibility for achieving high-performance vertical heterojunction optoelectronic devices [32–34]. Despite extensive research, the transient charge transport kinetics at the interface remain insufficiently explored [35–37]. This neglect often leads to serious interface composite phenomena and excessively high dark current, both of which fundamentally affect the self-powered switching performance of the device.

Previous studies have shown that the use of electron transport layer/hole transport layer (ETL/HTL) can significantly improve carrier extraction and suppress carrier recombination [38–40]. Nevertheless, current research mainly focuses on enhancing solar conversion efficiency, and direct comparative studies on the impact of the ETL layer on the performance of self-powered photodetectors are still relatively limited [41, 42]. Particularly in terms of dark current, zero-bias photodetection response, and imaging stability, systematic investigations are still lacking [43, 44].

Here, we designed and fabricated an $Au/WSe_2/MAPbBrI_2/ZnO$ /ITO vertical heterojunction array and systematically investigated the role of the electron transport layer ZnO in this vertical structure photodetector. This structure fully utilizes the p-type characteristic of WSe_2 and the strong light absorption ability of the perovskite, while introducing ZnO as the electron transport layer, aiming to achieve efficient carrier separation and extraction under zero bias. The study found that the ZnO layer can effectively suppress the dark current of the device and significantly enhance its self-powered optical response through achieving selective charge transport at the interface. To understand the physical mechanism, we compared the energy band alignment of the two device architectures. This analysis revealed that the incorporation of ZnO created a more favorable energy cascade, significantly facilitating interfacial electron extraction and thus improving the overall photoelectric performance. Based on the optimized device structure, we successfully achieved a self-powered imaging demonstration, verifying its potential in practical applications. These results underscore the pivotal role of interface engineering in modulating the performance of 2D/3D vertical heterojunctions, providing essential experimental evidence and theoretical frameworks for the development of future high-performance, energy-efficient photodetection systems.

2 | Results and Discussion

Reasonable material selection and interface design are crucial for realizing self-powered vertical heterojunction photodetectors. In this work, high-quality WSe_2 films were synthesized via chemical vapor deposition (CVD). In contrast, perovskite layers reported in previous studies are predominantly prepared by spin coating, a process that typically requires hydrophilic surfaces. However, the commonly employed plasma treatment to improve surface wettability inevitably damages the surface of WSe_2, leading to significant degradation of its electrical and optical properties. To overcome these limitations, a spray-coating method was adopted for the deposition of $MAPbBrI_2$ perovskite films. This approach effectively improves interfacial adhesion between the perovskite and WSe_2 while avoiding structural damage to the two-dimensional semiconductor, thereby providing a mild and controllable strategy for constructing vertical heterostructures.

Figure S1 illustrates the fabrication process of the vertical photodetector. Specifically, interdigitated electrodes were first patterned on a silicon substrate using standard photolithography, followed by magnetron sputtering of Cr/Au contacts. The CVD-grown WSe_2 film was transferred onto the pre-patterned electrodes via a wet-transfer process. This was followed by the sequential deposition of the $MAPbBrI_2$ perovskite, a ZnO electron transport layer, and the top ITO electrode, utilizing spray coating and magnetron sputtering, respectively (see Supporting Information for details). The stacked configuration of these functional layers is schematically illustrated in Figure 1a, while Figure 1b presents the final device array captured by an optical microscope. SEM observations (Figure 1c) further confirm a dense and uniform film morphology, validating the robustness of our scalable interface-stacking strategy for large-area photodetectors. The optical transmittance spectrum of the perovskite film exhibits strong absorption with a well-defined absorption edge in the visible range, confirming the suitability of $MAPbBrI_2$ as an efficient light-absorbing layer for visible photodetection (Figure 1d). The optical integrity of the WSe_2 monolayer was further corroborated by photoluminescence (PL) and Raman spectroscopy (Figure 1e,f).

Building upon the material and structural validation in Figure 1, we systematically evaluated the optoelectronic performance of the vertical WSe_2/perovskite photodetectors. Initial electrical characterization was performed to investigate the photoresponse of a single-pixel $Au/WSe_2/MAPbBrI_2/ZnO/ITO$ device under zero external bias.

Figure 2a presents the time-resolved photocurrent (I–t) responses of the vertical photodetector under green-light illumination with varying power densities at zero bias. The device exhibits clear

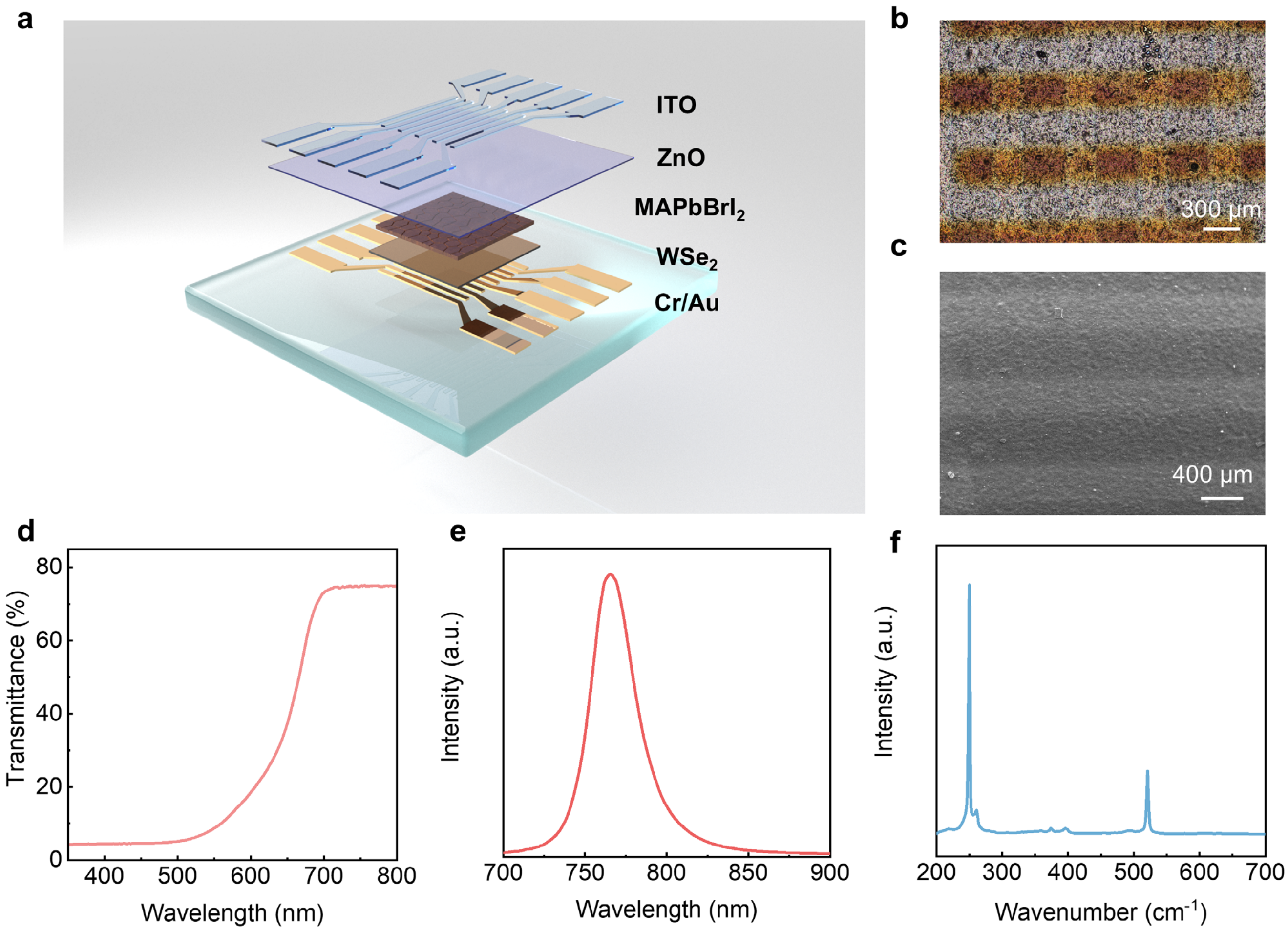

FIGURE 1 | (a) Schematic illustration of the vertical Au/WSe_2/$MAPbBrI_2$/ZnO/ITO photodetector architecture. (b) Optical microscopy image of the fabricated device. (c) Scanning electron microscopy (SEM) image of the device, showing the uniform and dense film morphology. (d) Optical transmittance spectrum of the $MAPbBrI_2$ perovskite film. (e) Photoluminescence (PL) spectrum of the CVD-grown WSe_2 film. (f) Raman spectrum of the WSe_2 film.

and reproducible switching behavior between the dark and illuminated states, indicating stable self-powered operation. As the incident optical power increases, the photocurrent exhibits a monotonic rise, whereas the dark current remains suppressed at a constant baseline. This disparity yields a robust on/off ratio reaching approximately four orders of magnitude. Similar trends in repeatable switching behavior are maintained under red-light illumination at zero bias. Although the red-light-induced photocurrent is slightly attenuated compared to its green-light counterpart, the consistent photoresponse across different wavelengths underscores the device's broadband detection capability, as evidenced by the spectral response range in Figure 2b.

The current–voltage (*I–V*) characteristics of the device under green-light illumination with different power densities are shown in Figure 2c. With increasing incident light intensity, the output current is gradually enhanced over the entire bias range. Notably, the *I–V* curves exhibit pronounced asymmetry, indicating the presence of a built-in electric field within the vertical heterojunction. To further clarify the influence of the ZnO electron transport layer on the interfacial carrier dynamics, the dark *I–V* characteristics of devices with and without ZnO were compared (Figure S2). The device with ZnO exhibits significantly suppressed reverse-bias leakage current and enhanced rectification behavior, indicating a more favorable band alignment and strengthened built-in electric field. This optimized junction configuration lays the foundation for the low dark current and stable self-powered operation observed in the vertical architecture. At an illumination power density of 2.708 mW cm^{-2}, the photocurrent reaches 11.5 nA. This internal electric field enables efficient carrier separation and underpins the observed self-powered photoresponse. This consistency extends to the 650 nm spectral regime, where the *I–V* profiles mirror the aforementioned self-driven characteristics (Figure 2d). Such wavelength-independent zero-bias response further supports the self-powered nature of the vertical heterostructure.

The response time of the device under green-light illumination is shown in Figure 2e. Upon periodic light on/off switching, the photocurrent exhibits clear and reproducible rise and decay behaviors. Quantitatively, the rise and decay times are determined to be approximately 0.61 and 0.55 s, respectively. This response behavior indicates effective separation and transport of photogenerated carriers facilitated by the vertical architecture. Figure 2f depicts the corresponding transient behavior under red-light illumination. A slight increase in the rise time (0.99 s) is observed,

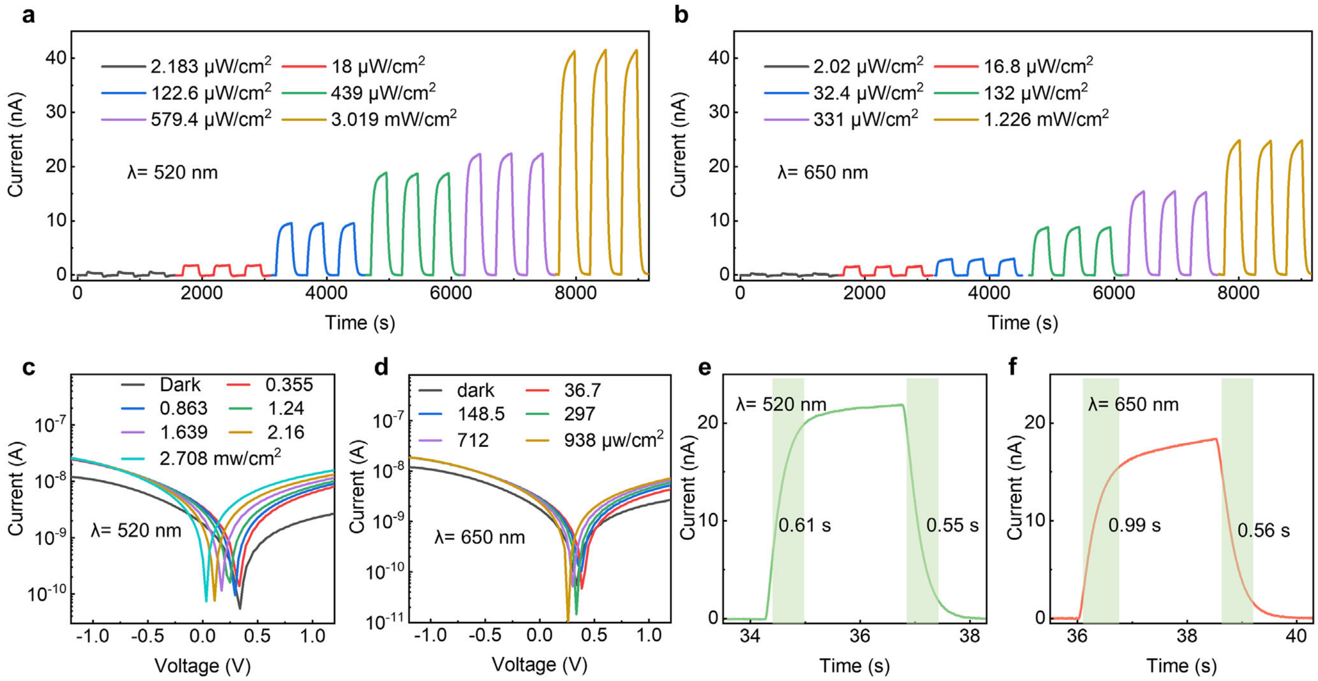

FIGURE 2 | Photoresponse characteristics of the Au/WSe_2/$MAPbBrI_2$/ZnO/ITO vertical photodetector under zero bias. (a) Time-resolved photocurrent (*I–t*) responses under 520 nm (green) illumination with different power densities. (b) *I–t* responses under 650 nm (red) illumination with different power densities. (c) Current–voltage (*I–V*) characteristics measured under green-light illumination with varying power densities. (d) *I–V* characteristics measured under red-light illumination with varying power densities. (e) Response time under green-light illumination, showing the corresponding rise and decay behaviors. (f) Response time under red-light illumination.

likely originating from wavelength-dependent absorption profiles and the associated carrier diffusion kinetics. Despite these minor variations, the device maintains robust and stable switching, confirming the reliability of its self-powered operation across the visible spectrum. The response time is likely governed by trap-assisted carrier dynamics in the perovskite layer and interfacial transport processes. In addition, the absence of external bias may further limit the carrier transport speed, leading to the observed response time.

To further evaluate the photodetection performance, key figures of merit, including responsivity (*R*) and specific detectivity (*D**) were calculated under 520 nm illumination at zero bias (Figure S3). The device exhibits a responsivity on the order of 10^{-3}–10^{-2} A W^{-1} and a detectivity on the order of 10^{11}–10^{12} Jones. These values are comparable to those reported for self-powered 2D/perovskite photodetectors. The corresponding temporal responses of the device without the ZnO layer are provided in Figure S4. Compared with the device with ZnO, slower and less pronounced switching behavior is observed, indicating that the ZnO layer facilitates more efficient carrier separation and transport.

To further elucidate the role of ZnO in enabling self-powered photodetection, Au/WSe_2/$MAPbBrI_2$ devices without the ZnO layer were fabricated using the same process flow, and their transient photocurrent responses under green and red illumination were systematically investigated (Figure S5). While the devices without ZnO counterparts retain repeatable on/off switching behavior, their photocurrent is significantly reduced compared to devices with ZnO. Specifically, under equivalent power densities, the elimination of ZnO results in a fourfold and sixteenfold reduction in red- and green-light photocurrents, respectively.

Figure 3a,b present the photocurrent (I_{ph}) as a function of incident optical power (*P*) plotted on double-logarithmic scales for devices with and without ZnO. In both cases, the photocurrent follows a sublinear power-law dependence ($I_{ph} \propto P^{\alpha}$), with similar α values of approximately 0.62–0.63. This similarity indicates that the two devices share comparable photocarrier generation mechanisms. However, the significantly lower absolute photocurrent observed in the device without ZnO suggests that the performance degradation primarily originates from inefficient charge extraction rather than limited optical absorption. To further substantiate this interpretation, the *I–V* characteristics of the device without ZnO under varying illumination intensities are provided in Figure S6. Compared with the device with ZnO, the device without ZnO exhibits significantly weaker photocurrent enhancement and less pronounced rectifying behavior under illumination, directly reflecting inefficient carrier extraction at the perovskite/ITO interface.

As shown in Figure 3c, under zero bias, the device without ZnO exhibits a markedly suppressed photocurrent together with a reduced on/off contrast. This performance decay signifies intensified interfacial recombination and suboptimal electron extraction at the perovskite/ITO junction when a selective transport medium is lacking. A comparison of dark current profiles (Figure 3d) further reveals that the device with ZnO maintains a significantly lower noise baseline. In contrast, the device without ZnO suffers from increased leakage, pointing toward severe interfacial carrier backflow and recombination

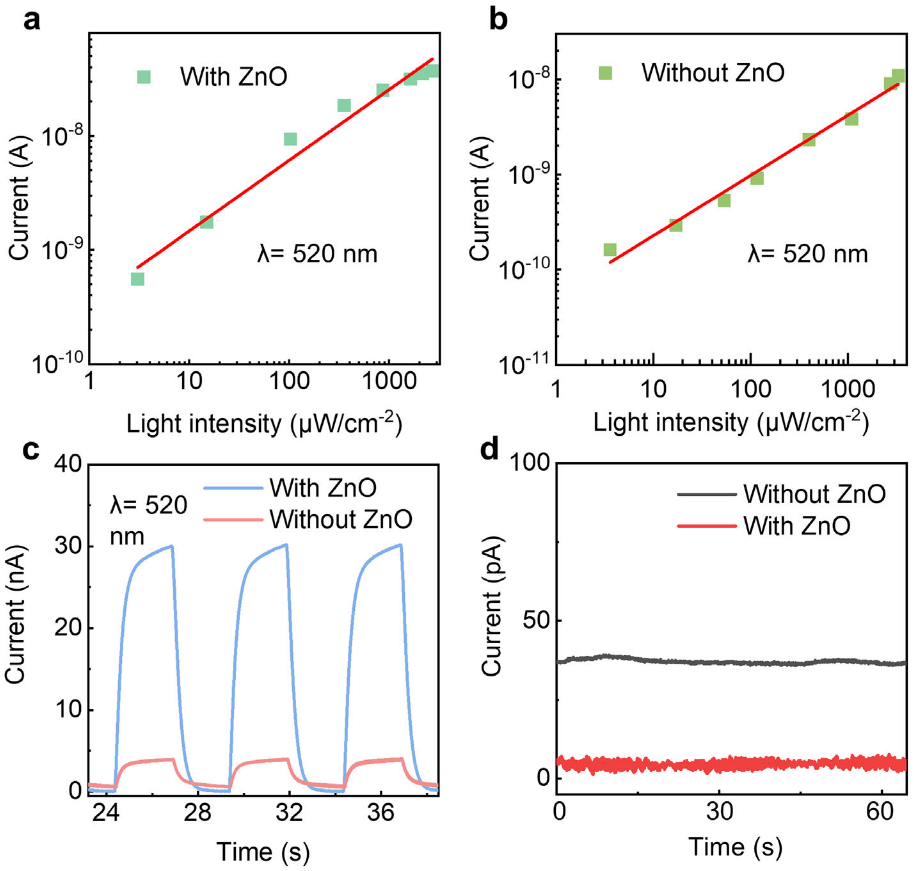

FIGURE 3 | Comparison of photoelectrical performance of vertical photodetectors with and without the ZnO electron transport layer. (a) Photocurrent (I_{ph}) as a function of incident optical power (P) for the device with ZnO plotted on a double-logarithmic scale. (b) Photocurrent versus optical power for the device without ZnO under the same illumination conditions. (c) *I–t* responses at zero bias for devices with and without ZnO under representative green-light illumination. (d) Dark current characteristics measured at zero bias for devices with and without the ZnO layer.

losses. Collectively, these results suggest that the incorporation of ZnO facilitates more efficient electron extraction at the perovskite/electrode interface and reduces interfacial recombination. The improved performance is associated with the combined effects of favorable band alignment and reduced interfacial recombination at the perovskite/ZnO interface. It is noted that the WSe_2/$MAPbBrI_2$ interface primarily governs hole transport, while the perovskite/ZnO/ITO interface plays a dominant role in electron extraction and recombination processes. The TRPL decay curves were fitted using a biexponential model, and the average lifetime (τ_{avg}) was extracted. After introducing the ZnO layer, the average lifetime decreases from ~1.05 to ~0.60 ns, indicating a faster decay process (Figure S7). This behavior is consistent with efficient interfacial electron extraction at the $MAPbBrI_2$/ZnO interface, which leads to photoluminescence quenching.

To clarify the intrinsic origin of the distinct photoresponse behaviors observed in devices with and without ZnO, schematic energy band diagrams of the vertical heterostructures are presented in Figure 4. As illustrated in Figure 4a, the WSe_2/$MAPbBrI_2$/ZnO vertical heterojunction exhibits favorable band alignment, giving rise to an effective built-in electric field at the interfaces. Upon illumination, photogenerated electrons in the perovskite layer are efficiently extracted toward the ZnO/ITO electrode, while holes are selectively transported toward the WSe_2/Au electrode. Acting as an electron transport layer (ETL), ZnO primarily serves as an electron-selective contact at the perovskite/ITO interface, which is consistent with more efficient electron extraction and reduced interfacial recombination. In contrast, the WSe_2/$MAPbBrI_2$ interface mainly governs hole transport within the vertical heterojunction. In addition to band alignment effects, the sputtered ZnO layer may also act as a physical buffer, mitigating direct contact between the perovskite and ITO and suppressing interfacial leakage pathways. Although sputtering may introduce interfacial defects or modifications, the overall improvement in device performance suggests that the beneficial effects of ZnO likely outweigh any potential sputtering-induced damage.

Conversely, the device without ZnO (Figure 4b) is plagued by an unfavorable energy band offset at the perovskite/ITO interface. The lack of an electron-selective medium creates a kinetic bottleneck for charge extraction, causing photogenerated electrons to stagnate at the junction. This localized charge accumulation leads to increased interfacial recombination losses. In addition, the direct contact between the perovskite and ITO may introduce leakage pathways and interfacial defects, further degrading device performance. While the hole-transport pathway toward the WSe_2/Au electrode may remain intact, the severely inhibited electron collection efficiency curtails the net carrier flux. Such interfacial impediments harmonize with the experi-

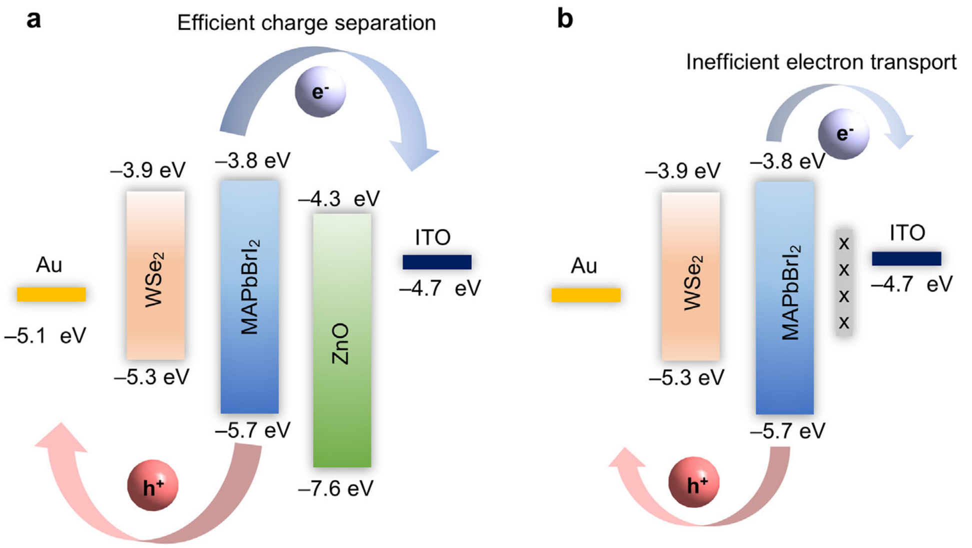

FIGURE 4 | Schematic energy band diagrams and charge transport mechanisms of the vertical heterojunction photodetectors. (a) Energy band alignment and carrier transport processes in the Au/WSe_2/$MAPbBrI_2$/ZnO/ITO device, illustrating efficient charge separation and selective carrier extraction under illumination. (b) Energy band diagram of the Au/WSe_2/$MAPbBrI_2$/ITO device without the ZnO layer, showing inefficient electron extraction and enhanced interfacial recombination.

mentally observed suppression of the zero-bias photoresponse in control devices. A comparison with representative 2D/perovskite photodetectors reported in recent literature is summarized in Table S1.

To verify the potential to realize reliable photon imaging capabilities, we further performed the characterizations of photoresponse for different pixels of our as-designed WSe_2/$MAPbBrI_2$/ZnO heterojunction array devices. We adopted a custom steel shadow mask with a pattern of "H" letter to produce a pattern of incident light [45]. The principle of measurement for array devices is shown in Figure 5a, in which the light out of the area of the shadow mask could get through and propagate into the pixels of devices, whereas other light would be blocked by the steel mask [44]. As a result, through the circuit of the probe station connected with the electrodes of devices, we can obtain the current mapping of different pixels by extracting photoresponses of corresponding device pixels. Before exploring the imaging effects of devices, we collected the data of dark current of every pixel.

In Figure 5b, the statistical distribution of dark current ranges from zero to about 20 pA, with a mean value of 5.99 pA, showing a relatively narrow variance of different pixels and a considerably low level. We randomly selected tens of pixels and carried out electrical measurements under illumination of a series of light intensities. As shown in Figure 5c, under the lights of 9.85, 30.5, 66, and 445 μW/cm^2, respectively, the chosen pixel set demonstrates relatively uniform photo currents. Despite some fluctuations, there is no overlap between the different light intensity levels, and the variations at some points were acceptably tolerable. Then we generalized the dark current of all pixels and response data under different light intensities, and performed statistical analysis (Figure 5d). Taking the dark current on the far left alone, it exhibits a significantly lower distribution level and is clearly distinguishable from the error bars of the photocurrent. On the other hand, all the error bars for different light intensities are very narrow, and their centers show an approximately linear increase with increasing light intensity. Therefore, these demographic studies of different pixels strongly confirm that our device can be used as a prerequisite for light intensity imaging.

The imaging consequences for "H" letter under different incident light intensities are shown in Figure 5e. The device successfully displayed the "H" pattern under all the light intensities tested, and importantly, the profile of the letter was discernible even at the lowest light intensity used. Under high light intensity, the patterned area exhibits a strong contrast with the surrounding dark area. It is worth noting that the dark areas of the device maintained a good, uniform, and low current distribution level throughout the process, which also indirectly verifies why our device can image well under weak light conditions. In addition, the long-term operational stability of the device was evaluated under continuous green-light illumination at zero bias (Figure S8). The photocurrent remains stable over 600 s without noticeable degradation, demonstrating the robustness of the vertical heterojunction and reliable self-powered operation. In summary, we have successfully demonstrated the application of array devices for light intensity imaging, showing promise for future reliable applications in display and communication for post-image-detection.

3 | Conclusion

In summary, we have demonstrated a self-powered vertical photodetector array based on an Au/WSe_2/$MAPbBrI_2$/ZnO/ITO heterostructure, specifically focusing on the synergistic modulation of interfacial charge transport. By integrating p-type WSe_2 with a broadband-absorbing mixed-halide perovskite and introducing ZnO as an electron transport layer, we achieved

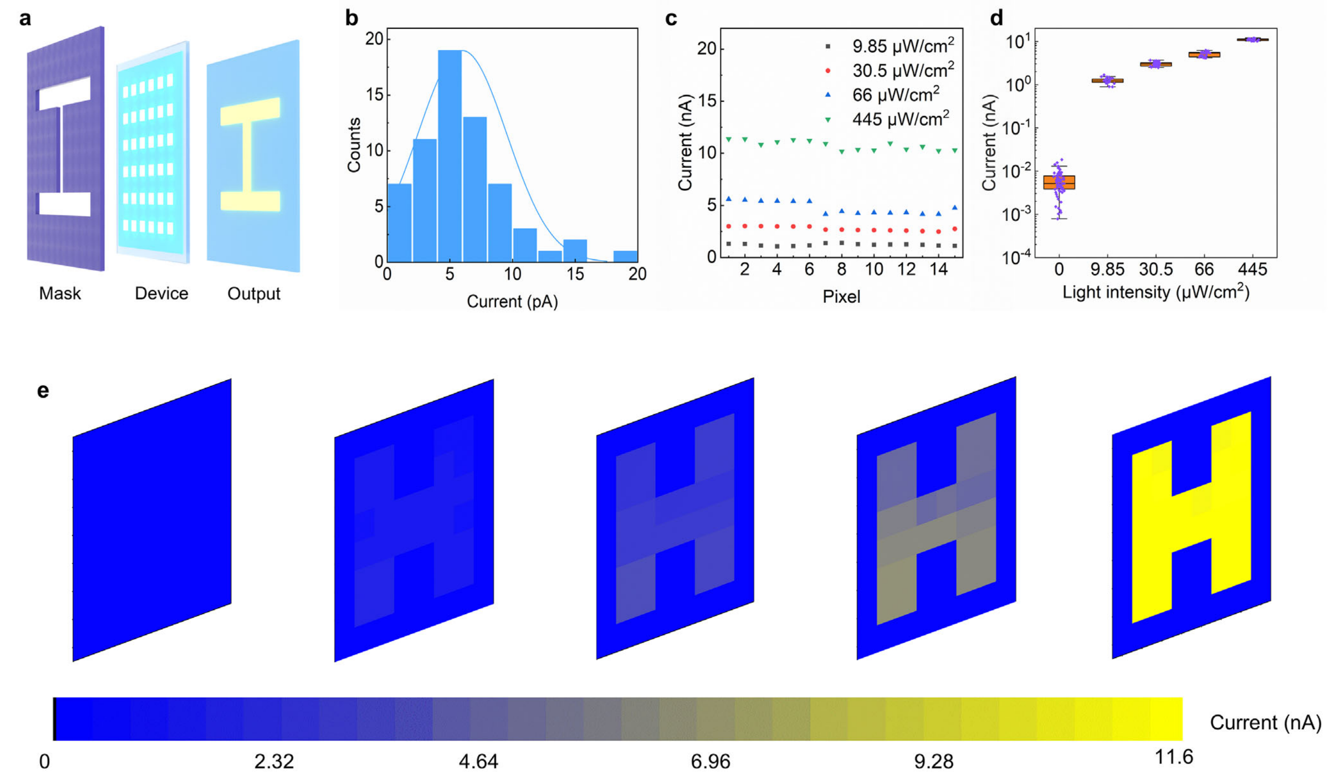

FIGURE 5 | Self-powered imaging performance of the Au/WSe_2/$MAPbBrI_2$/ZnO/ITO vertical photodetector array. (a) Schematic illustration of the imaging measurement setup using a patterned shadow mask. (b) Statistical distribution of dark current for individual pixels in the device array. (c) Photocurrent distributions of selected pixels under different illumination intensities. (d) Statistical analysis of photocurrent and dark current across the entire array under varying light intensities. (e) Photocurrent mapping images of the device array under patterned illumination, demonstrating reliable self-powered imaging capability.

improved carrier separation and extraction under zero external bias. Our comparative analysis delineates that the ZnO interlayer plays an important role in reducing dark current and enhancing zero-bias photocurrent in quenching dark current and amplifying the zero-bias photocurrent. The performance improvement is mainly attributed to enhanced electron extraction and reduced interfacial recombination at the perovskite/electrode interface, while the WSe_2 layer governs hole transport in the vertical heterostructure. Energy band analysis, together with electrical and TRPL results, supports the role of ZnO in facilitating selective carrier transport. Furthermore, the exceptional pixel-to-pixel uniformity and robust self-powered imaging performance underscore the practical viability of this architecture. Ultimately, the insights gained regarding interfacial band engineering and selective carrier transport provide a critical theoretical and experimental foundation for advancing the development of low-power, high-sensitivity integrated photodetection technologies.

4 | Experimental Section

4.1 | Preparation of $MAPbBrI_2$ Precursor Solution

$MAPbBrI_2$ precursor solution (0.5 M) was prepared by dissolving the corresponding precursors in a mixed solvent of DMF/DMSO/2-methoxyethanol (2-Me) with a volume ratio of 4:1:4. Specifically, MABr (33.6 mg), $PbBr_2$ (110.1 mg), MAI (95.4 mg), and PbI_2 (276.6 mg) were dissolved together with L-ascorbic acid (7.9 mg, corresponding to 5 mol% relative to Pb^{2+}) in 1.8 mL of the mixed solvent. The resulting solution was stirred until a clear and homogeneous precursor solution was obtained.

4.2 | Fabrication Process for Bottom Electrode

First, the bottom cross electrode pattern is fabricated on the SiO_2/Si substrate through lithography, and then the bottom electrode is prepared by magnetron sputtering. Cr/Au electrodes were deposited by magnetron sputtering under a high vacuum of 5×10^{-5} Pa with an Ar atmosphere, using a sputtering power of 70 W. Cr and Au were sputtered for 1 and 5 min, respectively, ensuring firm adhesion of the metal contacts to the substrate. Following electrode fabrication, the material was positioned via a localized transfer process.

4.3 | Fabrication of WSe_2/$MAPbBrI_2$ Photodetector Devices

The potassium hydroxide-assisted peeling technique was employed to transfer the WSe_2 film onto the Cr/Au cross electrodes on the Si/SiO_2 substrate. The specific operation was as follows: 1.5 g of polystyrene (PS) was dissolved in 8.5 g of toluene, and then spin-coated on the sample at a speed of 2000 rpm for 1 min. It was then baked at 120°C for 5 min. A polydimethylsiloxane (PDMS) template was used as the supporting layer, and the PS on the edge of the sapphire was gently scraped off to allow the moisture to penetrate. The stacked structure was immersed in a 1 M potassium hydroxide solution and soaked at 65°C for approximately 2 h to etch the sapphire interface. After the peeling of the WSe_2 film/PS/PDMS stacked structure, it was rinsed in deionized water and then transferred to the Cr/Au patterned SiO_2/Si target substrate. The PDMS was removed by heating to 130°C, and then PS was dissolved in toluene after cooling, leaving a clean WSe2 film precisely aligned in the expected device area.

Then, a volume of 70 μL of the $MAPbBrI_2$ precursor solution was loaded into the spray nozzle. The WSe_2 devices were placed on a hot plate maintained at 110°C, and the precursor solution was slowly and uniformly spray-coated onto the WSe_2 region to achieve a thickness-controlled and homogeneous perovskite film. Subsequently, the samples were annealed at 110°C for 20 min to promote solvent evaporation, enhance perovskite crystallization, and improve the interfacial contact between the $MAPbBrI_2$ layer and WSe_2. Subsequently, transparent indium tin oxide (ITO) top electrodes were deposited by magnetron sputtering to define the active device area and complete the vertical photodetector architecture. The ITO electrodes were deposited under an Ar flow rate of 35 sccm at a sputtering power of 70 W for 25 min.

4.4 | Fabrication of WSe_2/$MAPbBrI_2$/ZnO Photodetector Devices

After the preparation of the perovskite layer, a ZnO thin film was deposited onto the $MAPbBrI_2$ surface by magnetron sputtering to serve as the electron transport layer. The ZnO deposition was carried out under an argon flow rate of 35 sccm at a sputtering power of 70 W for 20 min. Subsequently, transparent indium tin oxide (ITO) top electrodes were deposited by magnetron sputtering to define the active device area and complete the vertical photodetector architecture. The ITO electrodes were deposited under an argon flow rate of 35 sccm at a sputtering power of 70 W for 25 min.

4.5 | Electrical Measurement

The photoresponse of the device was characterized by using a 520 and 650 nm laser as the light source. The *I–V* and *I–t* curves of the device were tested under dark conditions and different light intensities by a current amplifier (Stanford SR570), a function generator (Stanford DS345), and a probe station (Semiprobe M-6).

Acknowledgements

The authors thank the support of National Natural Science Foundation of China (No. 52125205, 52250398, U20A20166, 52172035, U25A20483 and 52203307), National key R&D program of China (2021YFB3200300 and 2021YFA1400502), Shenzhen Science and Technology Program (Grant Number. KQTD20170810105439418), Guangdong Major Project of Basic and Applied Basic Research (2021B0301030002), Natural Science Foundation of Beijing (L223006) and the Fundamental Research Funds for the Central Universities.

Conflicts of Interest

The authors declare no conflicts of interest.

Data Availability Statement

The data that support the findings of this study are available from the corresponding author upon reasonable request.

References

1. S. V. Grayli, T. Patel, B. van Kasteren, et al., “Near-Unity Absorption in Semiconductor Metasurfaces Using Kerker Interference,” *Nano Letters* 25, no. 23 (2025): 9362–9368, https://doi.org/10.1021/acs.nanolett.5c01777.

2. Y. Fan, W. Huang, F. Zhu, et al., “Dispersion-Assisted High-Dimensional Photodetector,” *Nature* 630, no. 8015 (2024): 77–83, https://doi.org/10.1038/s41586-024-07398-w.

3. W. Ran, Z. Ren, P. Wang, et al., “Integrated Polarization-Sensitive Amplification System for Digital Information Transmission,” *Nature Communications* 12 (2021): 6476, https://doi.org/10.1038/s41467-021-26919-z.

4. K. Zhao, J. Yang, P. Wang, et al., “β -Ga_2O_3 Nanoribbon With Ultra-High Solar-Blind Ultraviolet Polarization Ratio,” *Advanced Materials* 36 (2024): 2406559, https://doi.org/10.1002/adma.202406559.

5. W. Wu, X. Wang, X. Han, et al., “Flexible Photodetector Arrays Based on Patterned $CH_3NH_3PbI_{3-x}Cl_x$ Perovskite Film for Real-Time Photosensing and Imaging,” *Advanced Materials* 31 (2019): 1805913, https://doi.org/10.1002/adma.201805913.

6. J. He, R. Wei, S. Ge, et al., “Artificial Visual-Tactile Perception Array for Enhanced Memory and Neuromorphic Computations,” *InfoMat* 6, no. 3 (2024): 12493, https://doi.org/10.1002/inf2.12493.

7. Z. Yang, S. Huo, Z. Zhang, et al., “High-Precision Multibit Opto-Electronic Synapses Based on ReS_2/h-BN/Graphene Heterostructure for Energy-Efficient and High-Accuracy Neuromorphic Computing,” *Advanced Functional Materials* 35 (2025): 2509119, https://doi.org/10.1002/adfm.202509119.

8. J. Tang, X. Wang, J. Zhang, et al., “A Chalcogenide-Cluster-Based Semiconducting Nanotube Array With Oriented Photoconductive Behavior,” *Nature Communications* 12 (2021): 4275.

9. L. Guo, X. Liu, L. Gao, et al., “Ferro-Pyro-Phototronic Effect in Monocrystalline 2D Ferroelectric Perovskite for High-Sensitive, Self-Powered, and Stable Ultraviolet Photodetector,” *ACS Nano* 16, no. 1 (2022): 1280–1290, https://doi.org/10.1021/acsnano.1c09119.

10. L. Guo, H. Wang, Z. Xu, et al., “Interfacial Pyro-Phototronic Effect: A Universal Approach for Enhancement of Self-Powered Photodetection Based on Perovskites With Centrosymmetry,” *Advanced Functional Materials* 33 (2023): 2306526, https://doi.org/10.1002/adfm.202306526.

11. X. Han, J. Tao, Y. Liang, et al., “Ultraweak Light-Modulated Heterostructure With Bidirectional Photoresponse for Static and Dynamic Image Perception,” *Nature Communications* 15, no. 1 (2024): 10430, https://doi.org/10.1038/s41467-024-54845-3.

12. W. Wu, H. Lu, X. Han, et al., “Recent Progress on Wavelength-Selective Perovskite Photodetectors for Image Sensing,” *Small Methods* 7 (2023): 2201499, https://doi.org/10.1002/smtd.202201499.

13. X. Pan, J. Li, Z. Xu, et al., “A High Stretchability Micro-Crack Tactile Sensor System Based on Strain-Isolation Substrate,” *Materials Today Physics* 48 (2024): 101562, https://doi.org/10.1016/j.mtphys.2024.101562.

14. X. Liu, W. Zhang, X. Zhang, et al., “Transparent Ultrahigh-Molecular-Weight Polyethylene/MXene Films With Efficient UV-Absorption for Thermal Management,” *Nature Communications* 15 (2024): 3076, https://doi.org/10.1038/s41467-024-47432-z.

15. Y. Liang, Q. Lu, W. Wu, et al., “A Universal Fabrication Strategy for High-Resolution Perovskite-Based Photodetector Arrays,” *Small Methods* 7 (2023): 2300339, https://doi.org/10.1002/smtd.202300339.

16. Z. P. He, X. Han, W. Q. Wu, Z. S. Xu, and C. F. Pan, “Recent Advances in Bioinspired Vision Systems With Curved Imaging Structures,” *Rare Metals* 43, no. 4 (2024): 1407–1434, https://doi.org/10.1007/s12598-023-02573-w.

17. J. He, J. Huang, R. Li, et al., “Hysteresis-Free and Dynamically Resilient Strain Sensor Enabled by Interfacial Coordination,” *Science Advances* 12: aea2450, https://doi.org/10.1126/sciadv.aea2450.

18. M. Zhang, Z. Chi, G. Wang, et al., “An Irradiance-Adaptable Near-Infrared Vertical Heterojunction Phototransistor,” *Advanced Materials* 34 (2022): 2205679, https://doi.org/10.1002/adma.202205679.

19. H. Lu, W. Wu, Z. He, X. Han, and C. Pan, “Recent Progress in Construction Methods and Applications of Perovskite Photodetector Arrays,” *Nanoscale Horizons* 8 (2023): 1014–1033, https://doi.org/10.1039/D3NH00119A.

20. H.-C. Xu, Y. Liu, Y.-P. Mo, et al., “All-Fiber Anti-Jamming Capacitive Pressure Sensors Based on Liquid Metals,” *Rare Metals* 44 (2025): 4839–4850, https://doi.org/10.1007/s12598-024-03071-3.

21. J. Zhou, J. Lin, X. Huang, et al., “A Library of Atomically Thin Metal Chalcogenides,” *Nature* 556 (2018): 355–359, https://doi.org/10.1038/s41586-018-0008-3.

22. Z. Zhou, F. Hou, X. Huang, et al., “Stack Growth of Wafer-Scale van der Waals Superconductor Heterostructures,” *Nature* 621 (2023): 499–505, https://doi.org/10.1038/s41586-023-06404-x.

23. B. S. Wan, R. H. Zhou, W. K. Yang, et al., “Degradation of Electrical Performance of Few-Layer Tungsten Selenide-Based Transistors,” *Rare Metals* 44 (2025): 2534–2546, https://doi.org/10.1007/s12598-024-03147-0.

24. Z. Zhang, S. Huo, Q. Tian, et al., “Near-Perfect Standard Ternary Inverter Based on $MoTe_2$ Homojunction Anti-Ambipolar Transistor,” *Advanced Functional Materials* 35 (2025): 2424728, https://doi.org/10.1002/adfm.202424728.

25. E. Wang, J. Li, J. Li, Q. Cheng, X. Zhou, and H. Jiang, “Flattened and Broadband Mid-Infrared Super-Continuum Generation in As_2Se_3 Based Holey Fiber,” *Optical and Quantum Electronics* 51 (2019): 10, https://doi.org/10.1007/s11082-018-1722-7.

26. Q. Zhang, S. Zuo, P. Chen, and C. Pan, “Piezotronics in Two-Dimensional Materials,” *InfoMat* 3 (2021): 987–1007, https://doi.org/10.1002/inf2.12220.

27. P. Chen, J. Pan, W. Gao, et al., “Anisotropic Carrier Mobility From 2H WSe_2,” *Advanced Materials* 34 (2022): 2108615, https://doi.org/10.1002/adma.202108615.

28. L. Liu, T. Li, X. Gong, et al., “Homoepitaxial Growth of Large-Area Rhombohedral-Stacked MoS_2,” *Nature Materials* 24 (2025): 1195–1202, https://doi.org/10.1038/s41563-025-02274-y.

29. L. Bai, Z. Yang, J. Wen, et al., “Polarization Reversal Enhanced Intelligent Recognition in Two-Dimensional $MoTe_2$/GeSe Heterostructure,” *Chip* 4 (2025): 100143, https://doi.org/10.1016/j.chip.2025.100143.

30. G. Xue, B. Qin, C. Ma, P. Yin, C. Liu, and K. Liu, “Large-Area Epitaxial Growth of Transition Metal Dichalcogenides,” *Chemical Reviews* 124 (2024): 9785–9865, https://doi.org/10.1021/acs.chemrev.3c00851.

31. J. Song, T. Li, W. Li, et al., “Enabling Fast Photoresponse in Hybrid Perovskite/MoS_2 Photodetectors by Separating Local Photocharge Generation and Recombination,” *Nano Letters* 24 (2024): 14307–14314, https://doi.org/10.1021/acs.nanolett.4c03950.

32. Z. Xu, X. Han, W. Wu, et al., “Controlled On-Chip Fabrication of Large-Scale Perovskite Single Crystal Arrays for High-Performance Laser and Photodetector Integration,” *Light: Science & Applications* 12 (2023): 67, https://doi.org/10.1038/s41377-023-01107-4.

33. J. Sun, T. Li, L. Dong, et al., “Excitation-Dependent Perovskite/Polymer Films for Ultraviolet Visualization,” *Science Bulletin* 67 (2022): 1755–1762, https://doi.org/10.1016/j.scib.2022.08.009.

34. J. Lu, A. Carvalho, H. Liu, S. X. Lim, A. H. Castro Neto, and C. H. Sow, “Hybrid Bilayer WSe_2–$CH_3NH_3PbI_3$ Organolead Halide Perovskite as a High-Performance Photodetector,” *Angewandte Chemie International Edition* 55 (2016): 11945–11949, https://doi.org/10.1002/anie.201603557.

35. H. Wu, H. Si, Z. Zhang, et al., “All-Inorganic Perovskite Quantum Dot-Monolayer MoS_2 Mixed-Dimensional van der Waals Heterostructure for Ultrasensitive Photodetector,” *Advanced Science* 5 (2018): 1801219, https://doi.org/10.1002/advs.201801219.

36. C. Ma, Y. Shi, W. Hu, et al., “Heterostructured WS_2 /$CH_3NH_3PbI_3$ Photoconductors With Suppressed Dark Current and Enhanced Photodetectivity,” *Advanced Materials* 28 (2016): 3683–3689, https://doi.org/10.1002/adma.201600069.

37. Z. He, B. Sun, H. Lu, et al., “Focus-Tunable Real-Time Imaging System Based on Ultrathin Perovskite Curved Image Sensor With Hierarchical Mesh Design,” *Science Advances* 11, no. 36 (2025): adw7826, https://doi.org/10.1126/sciadv.adw7826.

38. Y. Ren, Y. Wang, Y. Fang, X. Jiang, K. Cheng, and Z. Du, “Regulation on Dual Interfaces of QD With ETL and HTL by Guanidine-Based Ligands Enable High-Performance Blue Quantum Dot Light-Emitting Diodes With 24.3% External Quantum Efficiency,” *Advanced Science* 12, no. 47 (2025): 12478, https://doi.org/10.1002/advs.202512478.

39. Y. Huang, T. Liu, C. Liang, et al., “Towards Simplifying the Device Structure of High-Performance Perovskite Solar Cells,” *Advanced Functional Materials* 30 (2020): 2000863, https://doi.org/10.1002/adfm.202000863.

40. X. Chen, W. Xu, N. Ding, et al., “Dual Interfacial Modification Engineering With 2D MXene Quantum Dots and Copper Sulphide Nanocrystals Enabled High-Performance Perovskite Solar Cells,” *Advanced Functional Materials* 30 (2020): 2003295, https://doi.org/10.1002/adfm.202003295.

41. J. Meng, Q. Li, J. Huang, C. Pan, and Z. Li, “Self-Powered Photodetector for Ultralow Power Density UV Sensing,” *Nano Today* 43 (2022): 101399, https://doi.org/10.1016/j.nantod.2022.101399.

42. Y. Peng, J. Lu, X. Wang, et al., “Self-Powered High-Performance Flexible GaN/ZnO Heterostructure UV Photodetectors With Piezo-Phototronic Effect Enhanced Photoresponse,” *Nano Energy* 94 (2022): 106945, https://doi.org/10.1016/j.nanoen.2022.106945.

43. H. Wang, X. Wang, Y. Chen, et al., “Extremely Low Dark Current MoS_2 Photodetector via 2D Halide Perovskite as the Electron Reservoir,” *Advanced Optical Materials* 8 (2020): 1901402, https://doi.org/10.1002/adom.201901402.

44. F. Li, Z. Xia, C. Pan, et al., “High Br—Content $CsPb(Cl_yBr_{1-y})_3$ Perovskite Nanocrystals With Strong Mn^{2+} Emission Through Diverse Cation/Anion Exchange Engineering,” *ACS Applied Materials & Interfaces* 10 (2018): 11739–11746, https://doi.org/10.1021/acsami.7b18750.

45. W. Q. Wu, C. F. Wang, S. T. Han, and C. F. Pan, “Recent Advances in Imaging Devices: Image Sensors and Neuromorphic Vision Sensors,” *Rare Metals* 43 (2024): 5487–5515, https://doi.org/10.1007/s12598-024-02811-9.

Supporting Information

Additional supporting information can be found online in the Supporting Information section.

Supporting File: smll73680-sup-0001-SuppMat.docx.